Progress In Electromagnetics Research C, Vol. 124, 53–68, 2022

Finite-Aperture Microwave Bessel Beams with Vortex Twisting, Fracturing, and Dynamic Phase-Shift Control

Vladimir Yurchenko[1, *], Mehmet Ciydem[2, 3], and Sencer Koc[4]

Abstract—Finite-aperture microwave vortex beams of various structures in the near-, middle-, and far-field propagation zones have been simulated. The decay of external sidelobes leading to the end of non-diffractive propagation within a fraction of the near-field zone is observed. A ring source of the vortex beams with phase-shift and frequency-sweep control of angular modes and polarization patterns through the use of patch antenna arrays of varying polarization is suggested. A new form of the beam wavefront variation with azimuthal undulation has been proposed that allows one to significantly diversify and dynamically control the beam structure. The consequences of a limited number of antenna patches in a circular array have been considered. The effects of a gradual drop of radiation power along the array and the use of multiple feed points for improving the beams have been simulated.

1. INTRODUCTION

Orbital angular momentum (OAM) vortex beams present a valuable tool in modern technology [1]. Non-diffractive propagation and conservation of topological structure are the distinctive features of the OAM beams useful for applications. Optical tweezers for manipulation of microscopic objects are a prominent example. Optical communication is another area where the OAM beams can increase the capacity of channels [2, 3], enhance the encoding, and provide other benefits [4]. Microwave vortex beams are also of interest for wireless communication [5–7] and radars [8–10].

Numerous techniques have been developed for generation of microwave vortex beams [11]. They involve twisted reflectors [12], traveling waves [13], metalenses [14, 15], metasurfaces [16, 17], antenna arrays [18–23], and other structures. At the same time, the issue of beam divergence has received less attention [24–26]. Non-diffractive beam propagation occurs only in the near field, which is quite limited in the microwave band. In the far field, the beams are divergent. Vortex beams are specified by helical wavefronts and zero on-axis power, with low-power paraxial zone expanding along with distance. So, exploring the near- to far-field transforms of the finite-aperture microwave vortex beams and seeking the ways for improving the beam characteristics is an important task, which is the aim of the given research.

In the research, a new form of OAM beam wavefront variation with azimuthal undulations is proposed. This allows one to significantly diversify and dynamically control the beam structures and quantitative characteristics. A possibility of tilting the beam and twisting it around its generatrix as a chief bearing axis provides an option for circularly scanning the vicinity of a target with the application of elements of synthetic aperture radar (SAR) technology. Degradation of the outer beam sidelobes when a limited number of antenna patches are used in a circular ring array has been simulated. Distortion of the beam shape due to the gradual drop of radiation power along the antenna array and the use of multiple feed points for restoring the beam quality have been considered.

Received 11 July 2022, Accepted 29 August 2022, Scheduled 12 September 2022
* Corresponding author: Vladimir Yurchenko (v.yurchenko@ostimteknik.edu.tr).
[1] Electrical and Electronics Engineering Department, Ostim Technical University, Ankara 06374, Turkey. [2] Electrical and Electronics Engineering Department, Gazi University, Ankara 06560, Turkey. [3] Engitek Engineering Technologies Ltd, Ankara 06460, Turkey. [4] Electrical and Electronics Engineering Department, Middle East Technical University, Ankara 06800, Turkey.

2. FINITE-APERTURE MICROWAVE BESSEL BEAMS

Consider microwave n-th order TE, TM Bessel beams $\mathbf{J}_n^{TE,TM}$ propagating in the positive direction of z-axis from a circular aperture of radius R_A centered at the origin in the plane $z = 0$. We compute both the near- and far-field finite-aperture Bessel beams using the formulations and notations of [27], which provide the integral presentations for all the field components at any $z > 0$ via the source field tangential components specified at $z = 0$.

In these formulations, e.g., the azimuthal component of the complex electric field amplitude of the infinite-aperture $\mathbf{J}_n^{TE}$ beam at $z = 0$ is

$$E_\varphi(r', \varphi') = E_{\varphi 0}\, J_n'(k_r r')\, \exp(in\varphi'), \tag{1}$$

where $J_n'(k_r r')$ is the derivative of the Bessel function $J_n(k_r r')$ over the argument; $k_r = 2\pi/\lambda_r$ is the radial wavenumber defined by the radial wavelength λ_r; $n = 0, \pm 1, \pm 2, \ldots$ is the beam angular order; and $E_{\varphi 0} = 1$ is the normalizing field amplitude (E_φ is the dominant field component at large $k_r r'$). Here, the plane-wave propagation wavenumber and wavelength are $k = 2\pi/\lambda$ and λ; the beam longitudinal wavenumber and wavelength are $k_z = 2\pi/\lambda_z$ and λ_z, respectively; $k^2 = k_z^2 + k_r^2 = (\omega/c)^2$, $\omega = 2\pi f$; f is the wave frequency; c is the speed of light; and typically, $\lambda \sim \lambda_z \ll \lambda_r$. For implementing the approach, a computer code has been created following the development of simulation software for electromagnetic modeling of dual-reflector radiotelescope on the ESA Planck Surveyor [28–31].

To introduce the finite-aperture beams, we include in the definition of $\mathbf{J}_n^{TE,TM}$ at $z = 0$ an apodization factor $s(r')$. It is applied to transverse field components, being $s = 1$ at $r' < R_S$, $s = 0$ at $r' > R_A$, and a smooth function $0 \le s(r') \le 1$ at $R_S \le r' \le R_A$ ($R_S = R_A - w$, w is the width of the transition zone). To satisfy Maxwell's equations at $z = 0$, the longitudinal fields acquire extra nonzero terms in the transition zone, although this is irrelevant for further calculations. Qualitative results do not depend on the choice of a smooth function $s(r')$ in a narrow transition zone, which is, typically, chosen to be $w \sim \lambda_r$ or $\lambda_r/2$ (electromagnetic vector fields of infinite-aperture Bessel beams, unlike the scalar ones in [32], never drop to exact zero out of axis).

Essential features of Bessel beams are their non-diffractive propagation in the near field (Fig. 1) and conversion into the annular beams in the far field (Fig. 2) [32]. Coordinates along the x_p and y_p axes on the far-field plane normal to the beam axis (z axis, $z \to \infty$) are defined in Fig. 2 as $x_p = \tan(\theta)\cos(\varphi)$ and $y_p = \tan(\theta)\sin(\varphi)$ where θ and φ are the polar and azimuthal angles, respectively.

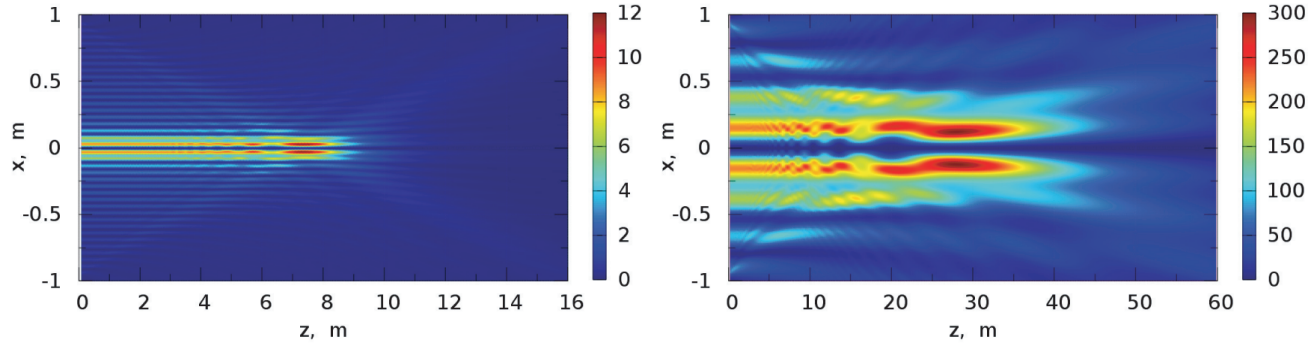


Figure 1. Near-field power flux $P_z(x, z)$ of microwave Bessel beam $\mathbf{J}_2^{TE}$ emitted from a circular aperture of radius $R_A = 100\lambda$ when (a) $\lambda_r = 10\lambda$ and (b) $\lambda_r = 50\lambda$ at $f = 30\,\text{GHz}$ ($\lambda = 1\,\text{cm}$, $R_A = 1\,\text{m}$, $w = 5\,\text{cm}$).

For conventional beams, the near- to far-field transition occurs at the distance $z_A \sim D_A^2/\lambda$ where D_A is the antenna diameter, $D_A \gg \lambda$ [27]. For the aperture-limited Bessel beams, the distance of non-diffractive propagation is evaluated as $z_B \sim R_A\lambda_r/\lambda$ where $\lambda \sim \lambda_z$, see Fig. 3(a) and Ref. [32].

Figure 3(a) shows the formation of the far-field wavefront that explains the annular patterns and the values of the divergence angles in the far field of the Bessel beams. It also explains the process of

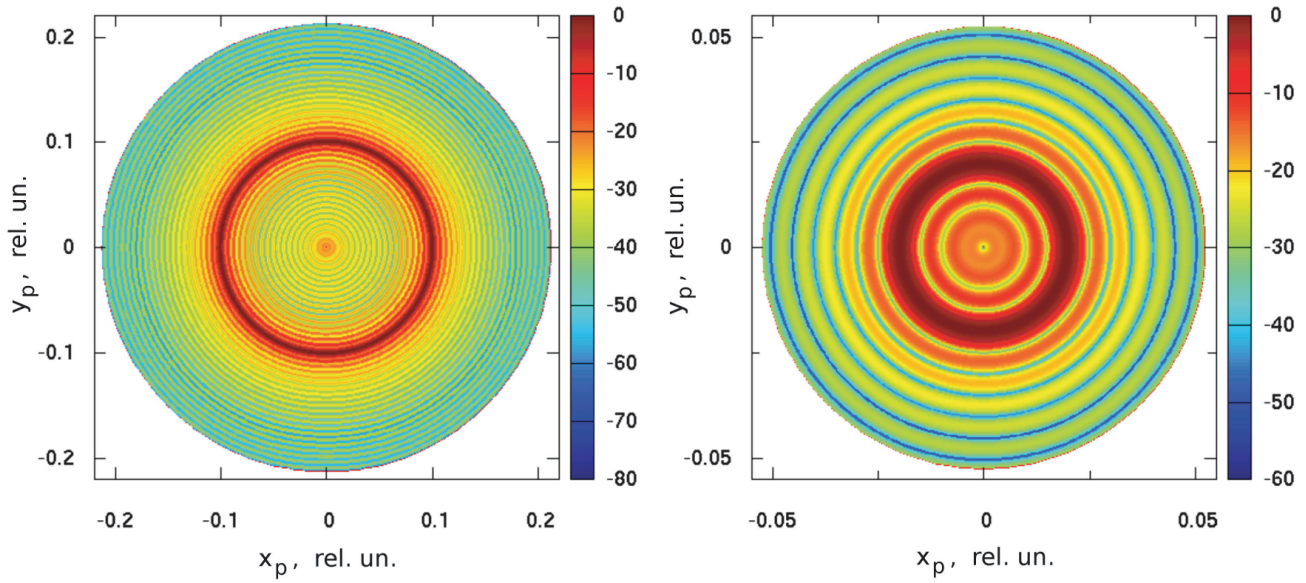


Figure 2. Far-field power patterns (a) and (b) of microwave Bessel beams $\mathbf{J}_2^{TE}$ whose near-field power plots are presented in Fig. 1(a) and (b), respectively.

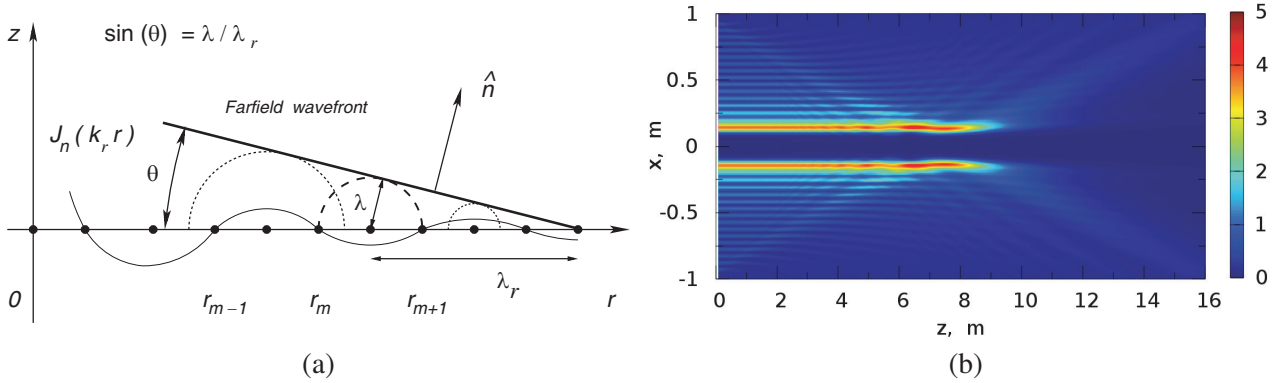


Figure 3. (a) Schematics of an annular beam formation due to the interference of partial waves of the Bessel beam sidelobes and (b) extinction of external sidelobes in the near-field propagation of the finite-aperture Bessel beam $\mathbf{J}_8^{TE}$ ($R_A = 1\,\text{m}$, $\lambda_r = 10\text{cm}$, $\lambda = 1\,\text{cm}$, $w = 5\,\text{cm}$).

extinction of external sidelobes in the near field of the finite-aperture Bessel beams, which is observed in Fig. 3(b) and the origin of the estimate for the value of z_B.

For generating high-quality Bessel beams of high azimuthal order $|n| \gg 1$ required for the accommodation of a large number of communication channels [2], one has to meet the conditions $R_A \gg \lambda_r \gg \lambda$ and use sufficient radius R_A providing $z_B \sim 1 - 10\,\text{km}$. In optics, one may use $R_A \sim 10\,\text{cm}$, $\lambda_r \sim 1\,\text{cm}$, $\lambda \sim 1\,\mu\text{m}$, and achieve $z_B \sim 1\,\text{km}$. In microwaves, at the frequency of, e.g., $f = 30\,\text{GHz}$ ($\lambda = 1\,\text{cm}$), the same range of z_B at the ratio $R_A/\lambda_r \sim 10$ requires the aperture radius $R_A \sim 10\,\text{m}$. The latter is not so easy to implement when the beam wavefront has to be controlled at the millimeter scale of accuracy. In general, because of conditions $\lambda \ll \lambda_r \ll R_A$, one has for the Bessel beams $z_B \sim z_A\lambda_r/4R_A \ll z_A$.

These circumstances stimulate further analysis of near- to far-field transitions of different kinds of vortex Bessel (quasi-Bessel) and annular (quasi-annular) microwave beams for extending their application range. At this stage, it is instructive to have a closer look on how the conversion of the

near-field Bessel beam to the far-field annular one occurs.

Basic features of the Bessel beams are explained by the properties of their sidelobes. According to the large-argument asymptotics of the Bessel functions $J_n(k_r r') \sim \sqrt{2/(\pi k_r r')}\cos(k_r r' - \pi/4 - n\pi/2)$ at $k_r r' \gg |n|$ (see, e.g., [27]), all the far sidelobes (i) have the same width $\lambda_r/2$, (ii) carry the same power flux P_z^S per each sidelobe ring, (iii) have the opposite phases of the fields in the adjacent rings, and (iv) make the total beam power proportional to R_A at $k_r R_A \gg |n|$.

As a result of the properties (ii) and (iii), destructive interference occurs for the partial waves of all the sidelobes in the direction of the z-axis. This leads to zero on-axis power in the far field of all the beams except for those of the angular order $n = \pm 1$, which have nonzero center lobe of circular polarization producing a minor on-axis field (see also derivations in Section 3). On the contrary, constructive interference occurs for the fields of all the sidelobes at the polar angle θ where $\sin(\theta) = \lambda/\lambda_r$ as shown in Fig. 3(a). The latter is identical to the condition

$$\tan(\theta) = \lambda_z/\lambda_r = k_r/k_z \tag{2}$$

formulated, e.g., in Ref. [32]. In this case, partial waves of adjacent sidelobes separated by the distance of $\lambda_r/2$, which have opposite phases on the aperture plane, acquire the same phases after one of the waves propagates an extra distance of $\lambda/2$ in the direction of θ.

The interference of partial waves in the near field produces two conical waves of which one is diverging, and the other is converging to the beam axis. The diverging wave disseminates the energy whereas the converging one maintains non-diffractive beam propagation until the last external sidelobe arrives at the beam axis. This explains the estimate of the non-diffractive range z_B specified above.

The estimate of non-diffractive propagation length z_B is consistent with simulations, with $z_B \sim 10\,\text{m}$ in Figs. 1(a) and 3(b), and $z_B \sim 40\,\text{m}$ in Fig. 1(b), whereas $z_A \sim 400\,\text{m}$ (the latter coincides with the Rayleigh length of the Gaussian beam of the waist radius $w_0 = 0.56D_A$). A more accurate estimate is $z_B \sim (R_A - r_{1n})\lambda_r/\lambda$ where r_{1n} is the radius defined by the first root of equation $J_n(k_r r_{1n}) = 0$. The estimate matches the simulations better, providing $z_B \approx 9.2\,\text{m}$, $z_B \approx 8.1\,\text{m}$, and $z_B \approx 30\,\text{m}$ for the relevant beams, respectively (see the near-field plots presented above).

Thus, the range of non-diffractive propagation of microwave Bessel beams specified by the length z_B is quite limited at the typical antenna sizes (pseudo-Bessel beams [19, 33] are no better in this respect). At the same time, the divergence angle in the far-field is also significant, being, e.g., $\theta = 5.7\,\text{deg}$ in the case of $R_A = 1\,\text{m}$, $\lambda_r = 0.1\,\text{m}$, and $\lambda = 0.01\,\text{m}$ ($f = 30\,\text{GHz}$) as shown in Figs. 2 and 4. In this case, the annular beam radius r_a grows, e.g., to $r_a = 100\,\text{m}$ already at the distance of $z = 1000\,\text{m}$. This makes any use of the far-field beams problematic when the entire beam structure has to be recorded and processed for applications.

3. MICROWAVE FAR-FIELD ANNULAR VORTEX BEAMS

Consider now the far-field structure of the finite-aperture Bessel beams in more detail in order to develop a basis for introducing a more generic kind of the OAM vortex beams presented in Section 4.

Figure 4 shows the far-field power plot $P(\theta)$ of beams (a) $\mathbf{J}_2^{TE}$ and (b) $\mathbf{J}_8^{TE}$ of Figs. 1(a) and 3(b), respectively, compared to $P_z(\theta, z)$ at $z = 100\,\text{m}$ and $z = 400\,\text{m}$, $R_A = 1\,\text{m}$, and $P_z(\theta, z)$ at $z = 400\,\text{m}$, $R_A = 0.5\,\text{m}$.

An important point illustrated by Fig. 4 is that the far-field pattern is formed, in fact, already at the length z_A where $z_A = 400\,\text{m}$ at $R_A = 1\,\text{m}$ in the examples above.

The other point is that the far field of the finite-aperture Bessel beam is the hollow conical (annular) beam having the apex angle θ defined by Eq. (2), though augmented with a series of sidelobes. The latter arise due to the finite aperture size, with the width of sidelobes being inversely proportional to the radius R_A as shown by the comparison of curves 3 and 4.

It is instructive to derive the far-field patterns of some canonical beams. In the equivalent electric current radiation model [27], let the complex-valued electric current density $\mathbf{j}_e(r', \varphi')$ on the aperture $z = 0$ be of the form

$$\mathbf{j}_e(r', \varphi') = \mathbf{g}_n e^{in\varphi'} = \left[g_{rn}(r')\hat{a}_r + g_{\varphi n}(r')\hat{a}_\varphi\right] e^{in\varphi'} \tag{3}$$

where $g_{rn}(r')$ and $g_{\varphi n}(r')$ are the complex-valued factors presenting the radial dependence of the radial and azimuthal current density components; $\hat{a}_r$ and $\hat{a}_\varphi$ are the radial and azimuthal unit vectors,

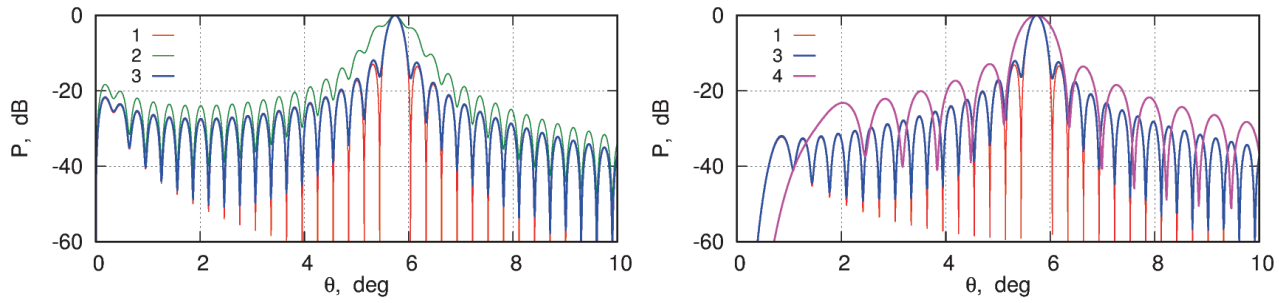


Figure 4. Far-field power patterns $P(\theta)$ (curves 1) of Bessel beams (a) $\mathbf{J}_2^{TE}$ and (b) $\mathbf{J}_8^{TE}$ of Figs. 1(a) and 3(b), respectively, when compared to $P_z(\theta, z)$ at $z = 100\,\text{m}$ and $z = 400\,\text{m}$, $R_A = 1\,\text{m}$ (curves 2 and 3, respectively) and $P_z(\theta, z)$ at $z = 400\,\text{m}$, $R_A = 0.5\,\text{m}$ (curve 4).

respectively; and n is the angular mode index. Then, the electric far-field $E_{\theta n}$ and $E_{\varphi n}$ components can be found as

$$E_{\theta n}(\theta, \varphi) = -\cos(\theta) e^{in\varphi} i^n \int_0^{R_A} \left[i g_{rn}(r') J_n'(\gamma r') + g_{\varphi n}(r')(n/\gamma r') J_n(\gamma r') \right] r' dr' \tag{4}$$

$$E_{\varphi n}(\theta, \varphi) = e^{in\varphi} i^n \int_0^{R_A} \left[g_{rn}(r')(n/\gamma r') J_n(\gamma r') + i g_{\varphi n}(r') J_n'(\gamma r') \right] r' dr' \tag{5}$$

where $\gamma = k \sin(\theta)$.

For the source current density vector

$$\mathbf{j}_e(r', \varphi') = \sum_n \mathbf{g}_n(r') e^{in\varphi'} \tag{6}$$

the total E_θ and E_φ far-field components are

$$E_\theta(\theta, \varphi) = \sum_n E_{\theta n}(\theta, \varphi) \qquad \text{and} \qquad E_\varphi(\theta, \varphi) = \sum_n E_{\varphi n}(\theta, \varphi). \tag{7}$$

If $g_{rn}(r')$ and $g_{\varphi n}(r')$ functions are linked as

$$g_{rn}(r') = \pm i g_{\varphi n}(r') \tag{8}$$

with the same sign for each angular mode, the current represents the source of circular polarization of $(+)$ or $(-)$ sign, respectively. In this case, the far-field of elliptical polarization is obtained for the total field and each angular mode, respectively, where

$$E_\theta(\theta, \varphi) \,/\, E_\varphi(\theta, \varphi) = \pm i \cos(\theta). \tag{9}$$

Circular polarization is observed on the beam axis when the field on the axis is nonzero (the latter occurs for the angular modes $n = \pm 1$, see derivations below).

If the radius-dependent current density factor of each angular mode is defined as

$$\mathbf{g}_n(r') = \mathbf{g}_{0n} \delta(r' - a)/a \tag{10}$$

at a certain $a > 0$, we obtain a source as a circular ring of radius $r' = a$ with the current density amplitude vectors

$$\mathbf{g}_{0n} = g_{0rn} \hat{a}_r + g_{0\varphi n} \hat{a}_\varphi. \tag{11}$$

In the case of a ring source of circular polarization, Eq. (9) is valid for either specific modes or the total field depending on whether the relations

$$g_{0rn} = \pm i g_{0\varphi n} \tag{12}$$

take place at the same sign for either the given modes or the entire set of modes, respectively.

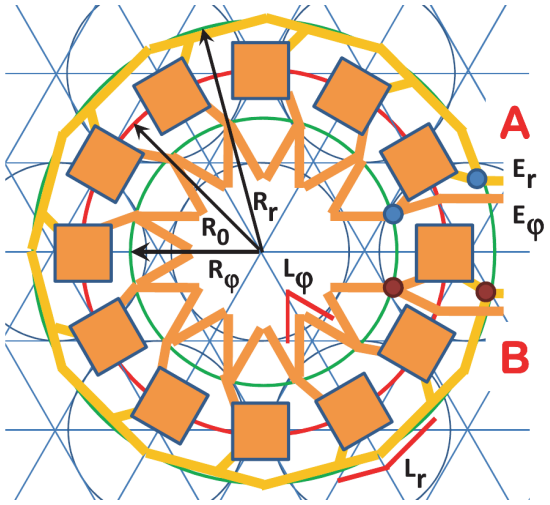


Figure 5. Schematics of a circular ring patch antenna array for the vortex beam generation with phase-shift and frequency-sweep control of angular modes and polarization pattern ($L_r = L_\varphi$, $E_r = \pm iE_\varphi$ for circular polarizations of $(+)$ and $(-)$ signs, respectively; switching between A and B feed points alters the sign of index n).

A ring source for exciting a vortex beam with phase-shift and frequency-sweep control of angular modes can be implemented as a patch antenna array presented in Fig. 5.

The drawing shows a small array of $N = 12$ patch antennas, each capable of launching the beams of two orthogonal polarizations when being excited with external feed signals E_r and E_φ. The signals are supplied at the feed points marked in either (A) blue or (B) brown color and delivered to every patch via two chains of microstrip lines shown as yellow and amber strips for each polarization, respectively. Switching the input signal between feed points A and B alters the sign of the beam index n (the opposite point is used in each case for diverting non-radiated power to an absorber; the intersection of strip lines at the feed point B can be avoided in 3D configuration of the feed lines).

When the effective lengths of microstrip lines L_r and L_φ are equal one to another and provide necessary phase delays $\Delta\Phi_n$ between patches at certain frequencies f_n, we can excite, through sweeping the frequency, the vortex beams of controllable angular order and polarization pattern by controlling the feed signals E_r and E_φ. The phase delays are defined by the difference between the length L_r and wavelength λ_S of the waves in the microstrip lines.

At the given frequency band $f_{\min} \le f \le f_{\max}$, when choosing the length $L_r = \lambda_S$ at the frequency $f_{\min}$, the angular order n is limited to the range $0 \le |n| \le M$ where the maximum order M is

$$M = \text{int}\left[(f_{\max}/f_{\min} - 1)N\right]. \tag{13}$$

With altering the sign of n, this provides the range of $2M + 1$ angular orders being available.

Equation (13) follows from the analysis of phase delays when sweeping the frequency. At the frequency $f_{\min}$ all the patches radiate in phase, and the beam of zero order is formed. With increasing the frequency, every next order n is achieved when the number of wavelengths fitting the entire array is increased by one. The maximum order M is obtained at the maximum frequency within the band when the integer number of wavelengths $N + M$ is still fitting the array length.

The antenna array is supposed to operate in the frequency band of $f = 24$–$28\,\text{GHz}$ where the optimal patch antenna size is $p = 3.14\,\text{mm}$ (these are the antennas replacing the design of Ref. [34] when moving in the Ka frequency band). The radii of relevant circles are, approximately, $R_\varphi = 8\,\text{mm}$, $R_0 = 12\,\text{mm}$, and $R_r = 16\,\text{mm}$ at the relative dielectric constant of substrate $\varepsilon_r = 2.2$.

The array can be approximated by the ring model of Eq. (10) where $a = R_0$. At the given number of patches, the maximum order is $M = 2$. If the values of L_r are adjusted properly ($L_r \approx 7.2\,\text{mm}$), the array produces the beams of the orders of $n = 0, \pm1, \pm2$ at the frequencies of $f_0 = 24\,\text{GHz}$, $f_{\pm1} = 26\,\text{GHz}$, and $f_{\pm2} = 28\,\text{GHz}$ when the phase delays between the adjacent patches are $\Delta\Phi_n = 2\pi(1+n/N)$, respectively.

Should the array contained $N = 120$ patches, it would have the outer diameter of $D_r = 320\,\text{mm}$ providing $M = 20$ and the total number of modes $2M + 1 = 41$.

Increasing the radius of the array and the number of patches allows one to make a ring source for the beams of sufficiently high orders, which are eagerly scanned by sweeping the frequency. Using a set of K concentric arrays with adjusted radii R_{0k}, numbers of patches N_k, phases and amplitudes of E_{rk} and $E_{\varphi k}$ signals, $k = 1, 2, \ldots, K$, one can generate the beams of complicated radial and axial power, phase, and polarization patterns, which are dynamically controlled via the phase shifters by the amplitudes and phases of E_{rk} and $E_{\varphi k}$ excitation waves.

The benefit of concentric ring excitation is that the field is controlled in terms of quantities, which specify the radial and angular parameters of the radiating source that, in due turn, corresponds to the far-field control directly in terms of the spherical coordinates of beams.

The main factor in defining the source model is the accurate control of phases of the antenna elements while the power may be controlled less rigorously. The approach is justified when the radiation efficiency of each element is small. If it is not so, a partial solution could be to create a few feed points along the array (A_1 and B_1, A_2 and B_2, etc.) with properly adjusted phases and powers. Relevant simulations are discussed in Section 4. Equalizing the power of antenna patches may be achieved by adjusting the coupling of patches to microstrip lines (optimizing the feeds of separate patches). In general, each element would require a separate feed, which is a complicated solution, though the difficulty is of the same kind as for any active phased array antenna system.

Returning to the beams of ring sources specified by Eq. (10) and considering a single mode of the order n, we can find explicit far-field solutions. In the case of a ring source of (+) or (−) circular polarization specified by Eq. (12), we obtain

$$E_{\varphi n}(\theta, \varphi) = \pm i\, e^{in\varphi}\, i^n\, g_{0\varphi n} J_{n\pm1}(\gamma a) \tag{14}$$

where $\gamma = \gamma(\theta) = k \sin(\theta)$ and $E_{\theta n}(\theta, \varphi)$ is provided by Eq. (9).

In the case of a ring source with only radial g_{0rn} current component ($g_{0\varphi n} = 0$), we obtain

$$E_{\varphi n}(\theta, \varphi) = n\, e^{in\varphi}\, i^n\, g_{0rn}\, J_n(\gamma a)/\gamma a \qquad \text{and} \qquad E_{\theta n}(\theta, \varphi) = -i \cos(\theta)\, e^{in\varphi}\, i^n\, g_{0rn}\, J'_n(\gamma a). \tag{15}$$

This is the far-field that has a TM-kind Bessel-beam structure where $E_{\theta n}(\theta, \varphi)$ is the dominant component at large polar angles θ when $ka \gg |n|$.

Finally, in the case of a ring source specified with only azimuthal $g_{0\varphi n}$ current component ($g_{0rn} = 0$),

$$E_{\varphi n}(\theta, \varphi) = -i\, e^{in\varphi}\, i^n\, g_{0\varphi n}\, J'_n(\gamma a) \quad \text{and} \quad E_{\theta n}(\theta, \varphi) = -n \cos(\theta)\, e^{in\varphi}\, i^n\, g_{0\varphi n}\, J_n(\gamma a)/\gamma a. \tag{16}$$

This is the far-field that has a TE-kind Bessel-beam structure where $E_{\varphi n}(\theta, \varphi)$ is the dominant component at large θ and $ka \gg |n|$.

Thus, for producing either the TM- or TE-kind Bessel beam patterns of the angular order n in the far filed of transmitting antenna, the latter should be made as a ring source generating only the radial or azimuthal current at the given order n of the phase factor $e^{in\varphi}$, respectively. At the same time, for creating the far-field beam of nearly-circular polarization of the same (+) or (−) sense through the entire beam of the Bessel-kind power profile at a certain angular order n (the power profile would be of the order $n \pm 1$), a ring source of the relevant circular polarization (emitted at each radiating point) and proper angular order has to be used.

An example of the far-field power patterns of beams created by the ring source of radius $a = 1\,\text{m}$ at the order $n = 8$ and frequency $f = 30\,\text{GHz}$ in the case of azimuthal (TE), radial (TM), and (+) and (−) circular polarizations (curves 1 to 4, respectively) is shown in Fig. 6(a).

For the canonical microwave Bessel beams emitted from the aperture of unlimited radius $R_A \to \infty$ at $z = 0$, Eqs. (4) and (5) allow one to derive exact solutions for the far-field $E_{\theta n}$ and $E_{\varphi n}$ components. For the integrity of presentation, we briefly consider the basic steps of derivation.

In the case of TE beams of the angular order n, the equivalent electric current density factors are

$$g_{rn}(r') = (n/k_r r')\, J_n(k_r r')\, g_0^{TE} \qquad \text{and} \qquad g_{\varphi n}(r') = i\, J'_n(k_r r')\, g_0^{TE}. \tag{17}$$

This reduces Eqs. (4) and (5) to the form

$$E_{\theta n}(\theta, \varphi) = -i \cos(\theta)\, e^{in\varphi}\, i^n\, g_0^{TE}\, I_{\theta n} \qquad \text{and} \qquad E_{\varphi n}(\theta, \varphi) = e^{in\varphi}\, i^n\, g_0^{TE}\, I_{\varphi n} \tag{18}$$

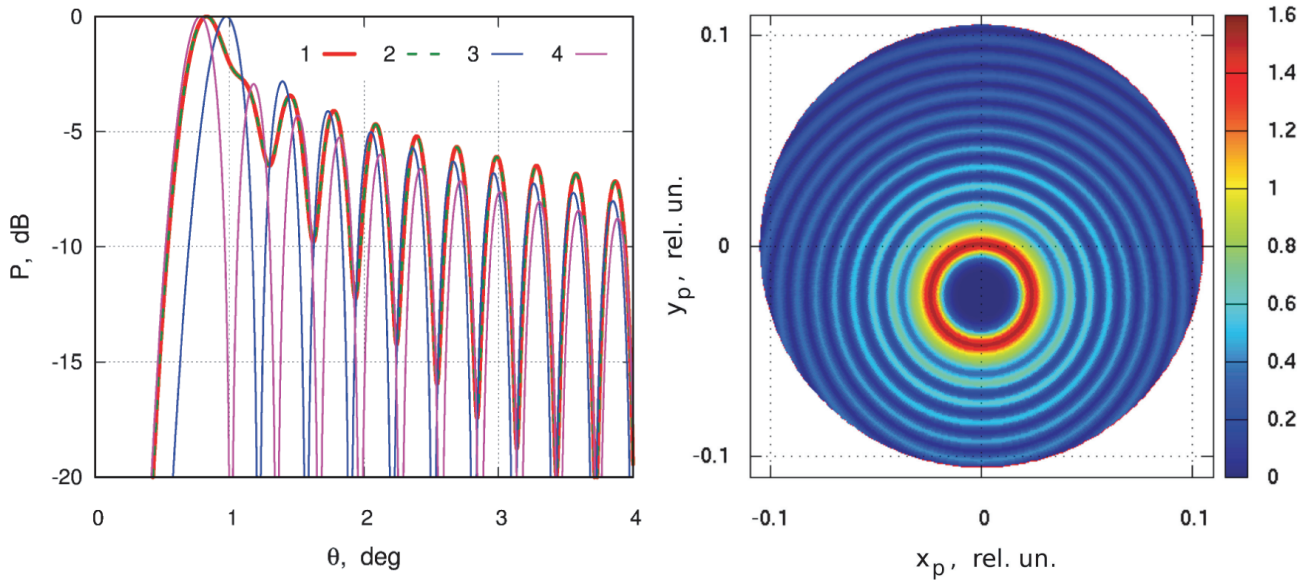


Figure 6. Far-field power patterns of (a) conical beams from the ring sources ($n = 8$, $a = 1\,\text{m}$, $\lambda = 1\,\text{cm}$) of azimuthal (TE), radial (TM), and circular polarizations of (+) and (−) signs (curves 1 to 4, respectively) and (b) a tilted beam from the ring source defined by Eq. (11) at $g_{0rn} = 0$ (azimuthal polarization, $a = 0.6\,\text{m}$, $\lambda = 1\,\text{cm}$) with the phase factor of Eq. (24) at $n = 8$, $m = 1$, $s = 2.8$, $\tau = 0$.

where

$$I_{\theta n} = \int_0^{R_A} \left[(n/k_r r')\, J_n(k_r r') J_n'(\gamma r') + (n/\gamma r')\, J_n'(k_r r') J_n(\gamma r') \right] r' dr' \tag{19}$$

$$I_{\varphi n} = \int_0^{R_A} \left[(n^2/k_r \gamma\, r'^2)\, J_n(k_r r') J_n(\gamma r') + J_n'(k_r r') J_n'(\gamma r') \right] r' dr'. \tag{20}$$

In the limit of $R_A \to \infty$, the integrals $I_{\theta n}$ and $I_{\varphi n}$ due to the orthogonality of the Bessel functions could only be nonzero under the condition $k_r = \gamma$, which is identical to Eq. (2). This defines the angle $\theta = \theta_a$ for constructive interference of the partial waves of beam sidelobes, see Fig. 3(a). In this way, the integrals $I_{\theta n}$ and $I_{\varphi n}$ acquire the δ-function factor in θ to become of the form

$$I_{\theta n} = I_{0\theta n}\delta(\theta - \theta_a) \qquad \text{and} \qquad I_{\varphi n} = I_{0\varphi n}\delta(\theta - \theta_a) \tag{21}$$

where $I_{0\theta n} = I_{\theta n}$ and $I_{0\varphi n} = I_{\varphi n}$ at $k_r = \gamma$. Then, the integral $I_{0\theta n}$ is reduced to

$$I_{0\theta n} = (n/2k_r)\left[J_n^2(k_r R_A) - J_n^2(0)\right] \to 0 \tag{22}$$

at $k_r R_A \to \infty$. At the same time, the integral $I_{0\varphi n}$ grows asymptotically as $I_{0\varphi n} = R_A/\pi k_r$ with increasing R_A at $k_r R_A \gg 1$. This is the result of a linear growth of total power flux P_0 of the source beam with increasing R_A at the constant value of g_0^{TE}. Should the power flux P_0 be constant instead of g_0^{TE}, the integral $I_{0\varphi n}$ would tend to a constant nonzero value for large $k_r R_A$.

Thus, in the far field of the TE Bessel beam emitted from an infinite aperture, the only nonzero E field component is $E_{\varphi n}$, i.e., the azimuthal component, and the nonzero value of $E_{\varphi n}$ is only obtained at the polar angle defined by Eq. (2). It means that the TE Bessel beam in the far-field domain is a hollow conical beam of azimuthal polarization, whose angular dependence of the $E_{\varphi n}$ component is of the form

$$E_{\varphi n}(\theta, \varphi) \sim \delta(\theta - \theta_a)\, e^{in\varphi} \tag{23}$$

where θ_a is the angle satisfying Eq. (2). In the case of TM Bessel beams emitted from an infinite aperture, the same is true for the $E_{\theta n}$ field. Then, Eq. (23) where $E_{\varphi n}$ is replaced by $E_{\theta n}$ defines the polar component instead of the azimuthal one.

4. DYNAMIC PHASE-SHIFT CONTROL OF MICROWAVE VORTEX BEAM PATTERNS

Far-field conical beams of either the Bessel or ring sources are specified by the apex angle θ_a, which could be significant while the power on axis is zero. For sensing a point-like target and its vicinity with such a beam, it could be useful to tilt the beam by the angle θ_a with respect to the target as shown in Fig. 6(b) and start scanning the far-field domain by turning the beam about its generatrix, which is pointing towards the target at $\theta = 0$.

There could be two options for the beam turning frequency Ω. If Ω is low, the sensing occurs with the actual beam that moves as the function of time. If Ω is high, the response could be formed with an effective beam obtained as the average of the original beam over the turning angle about generatrix as the axis. The SAR technology could be applied to the circular scanning described above.

For making the beam to turn around generatrix and, if needed, evolve in a more complicated manner, the angular phase factor $f_n(\varphi')$ of the current density function $\mathbf{j}_e(r', \varphi')$ in Eq. (3), instead of being of the form $f_n(\varphi') = \exp(in\varphi')$, should be of the kind

$$f_n(\varphi'; m, s, \tau) = \exp\left\{i\left[n\varphi' + s\pi \sin\left(m(\varphi' - \tau)\right)\right]\right\} \tag{24}$$

where s is the parameter defining the beam tilting angle, m the angular order of the phase front undulations producing the tilts ($m \geq 0$), and $\tau = \tau(t)$ the azimuthal angle defining the direction of the beam tilt as the function of time t. For the uniform turning of the beam (twisting the vortex at the angular frequency Ω), one has to define $\tau(t) = \Omega t$.

Some examples of the far-field patterns of beams of the ring sources with phase factor of Eq. (24) at $a = 0.6\,\text{m}$, $\lambda = 1\,\text{cm}$, $\tau = 0$ are shown in Figs. 7 and 8. Near-field propagation of beams of Figs. 8(a) and (b) in the domain close to the source aperture ($z \leq 5\,\text{m}$) is shown in Figs. 9 and 10.

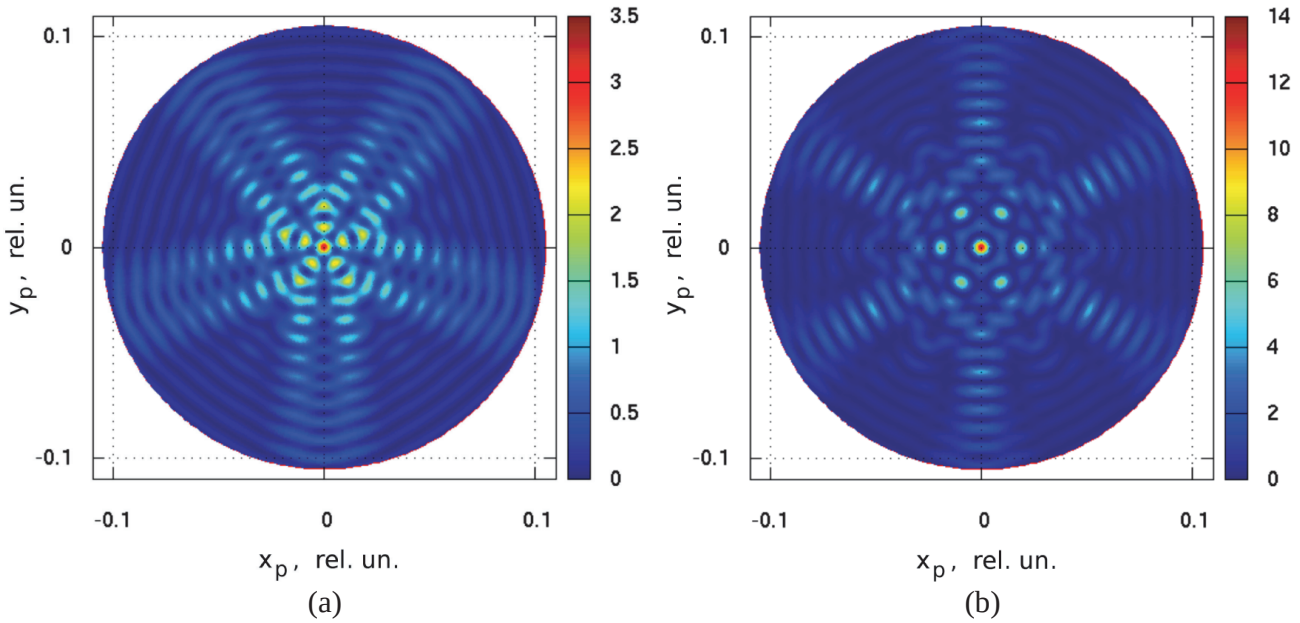


Figure 7. Fractured far-field power pattern of the beam of a ring source defined by (a) Eq. (11) at $g_{0rn} = 0$ (azimuthal polarization) with the phase factor of Eq. (24) at $n = 4$, $m = 5$, $s = 0.5$ and (b) Eq. (12) (circular polarization of $(-)$ sign) with the phase factor of Eq. (24) at $n = 7$, $m = 6$, $s = 0.5$.

The undulation of helical wavefront defined by Eq. (24) at $m \neq 1$ produces a split of the original n-th order beam into m sub-beams, each being tilted in a symmetric manner with respect to the twist axis $\theta = 0$. A central beam of the relevant order, either the vortex one (Fig. 8(a)) or not (Figs. 7 and 8(b)), with or without additional sub-structure, could also appear in this process.

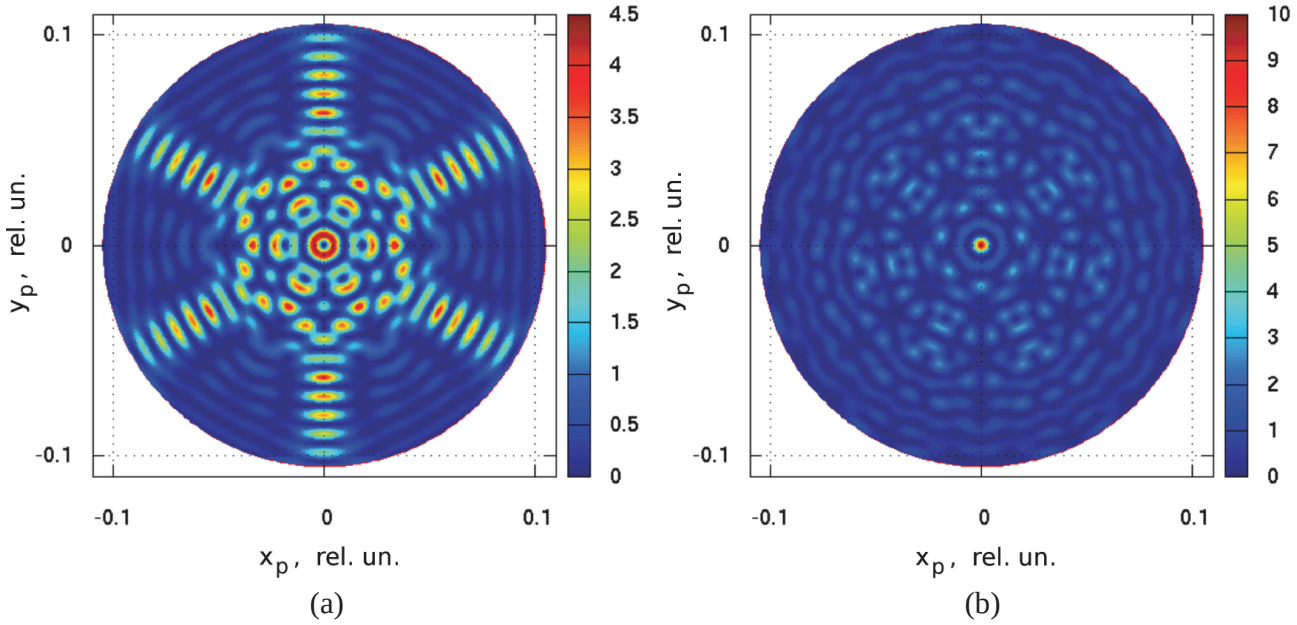


Figure 8. Fractured far-field power pattern of the beam of a ring source defined by Eq. (12) (circular polarization of $(-)$ sign, $a = 0.6\,\mathrm{m}$) with the phase factor of Eq. (24) at (a) $n = 8$, $m = 6$, $s = 0.5$ and (b) $n = 8$, $m = 7$, $s = 0.8$.

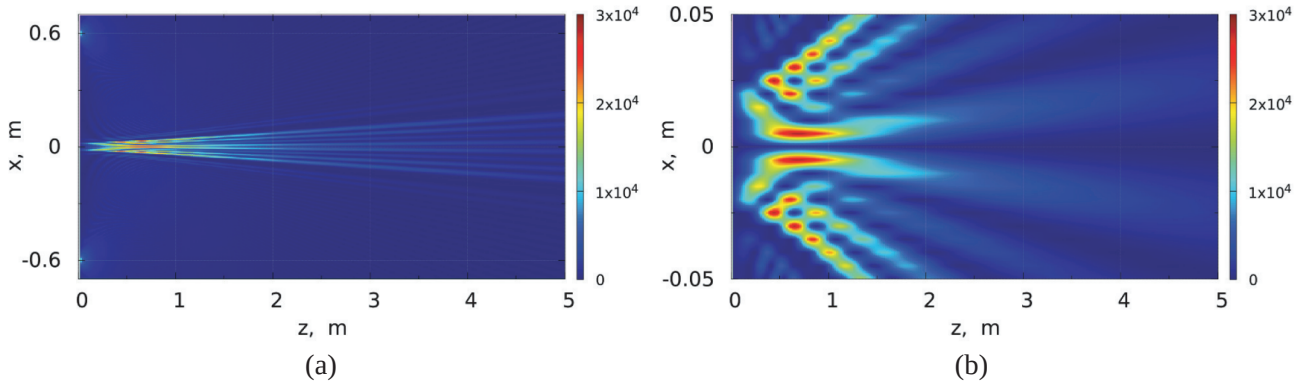


Figure 9. Near-field power flux $P_z(x, z)$ of the beam of Fig. 8(a) when (a) plotted at $|x| \le 0.7\,\mathrm{m}$ and (b) zoomed into $|x| \le 0.05\,\mathrm{m}$ ($a = 0.6\,\mathrm{m}$).

The emergence of m sub-beams could be understood as a result of interference of m tilted beams of the kind as shown in Fig. 6(b) where each beam is tilted in its own direction. Then, superposition of all the beams produces an m-th order power pattern in the total beam.

The apex angle of annular beams, when being measured from the beam axis to the sidelobe of maximum power, is smaller for the ring sources than the aperture Bessel beam emitters, see Figs. 4 and 6(a). For the beams of high index value, the apex angle increases almost in proportion to $|n|$ while the power flux at any fixed angle inside the vortex drops rapidly, being zero at the beam axis.

The beams of the lowest vortex order l ($l = 1$ at $n = 2$ for the ordinary beam of circular polarization of (-) sign and, e.g., $n = 8$, $m = 6$ for the fractured beam in Fig. 8(a)) have $\theta_a = 0.278\,\mathrm{deg}$ at $a = 0.6\,\mathrm{m}$, $\lambda = 1\,\mathrm{cm}$. In this case, the two identical ring antennas, when being used as the transmitting and receiving ones, being centered at the same axis, which is normal to both the antenna planes, would operate at the optimal conditions at the distance $z = 123\,\mathrm{m}$ ($z_A = 144\,\mathrm{m}$). At the same time, at the distance of $z = 1\,\mathrm{km}$, the optimal radius of the receiving antenna would have to be $a = 5\,\mathrm{m}$.

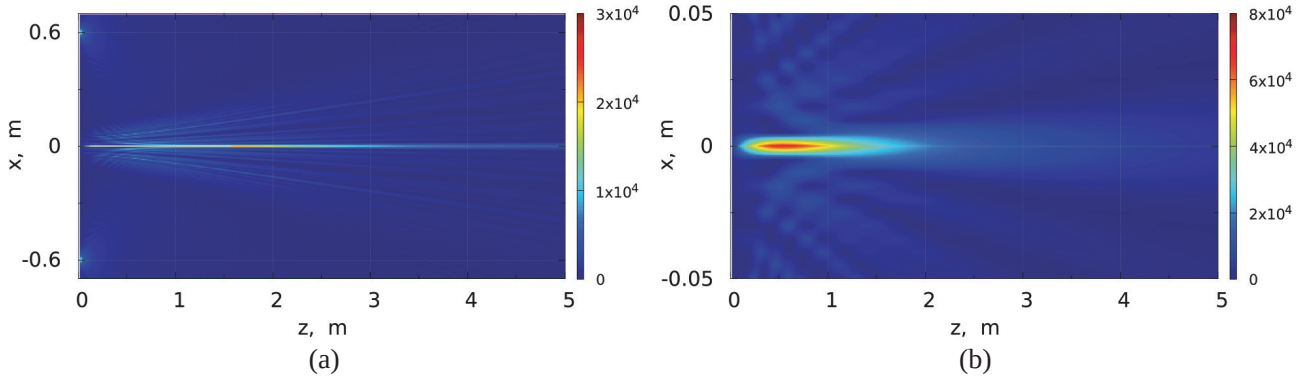


Figure 10. Near-field power flux $P_z(x, z)$ of the beam of Fig. 8(b) when (a) plotted at $|x| \leq 0.7\,\mathrm{m}$ and (b) zoomed into $|x| \leq 0.05\,\mathrm{m}$ ($a = 0.6\,\mathrm{m}$).

Figures 9 and 10 demonstrate near-field propagation of beams whose far-field patterns are presented in Figs. 8(a) and 8(b), respectively. They show that the far fields of beams are formed starting from very compact spots on the beam axis nearly at the ring aperture where extreme power fluxes appear due to constructive interference of waves emitted from all the points of ring sources.

For the better understanding of spatial structure of twisted and fractured beams, Fig. 11 shows the phase patterns of the E_{x_p} far-field component in the beams of (a) Fig. 8(a) and (b) Fig. 8(b), respectively. Here, E_{x_p} is the x_p component of the projection of the **E** vector on the far-field plane normal to the z axis where the x_p axis corresponds to the azimuthal angle $\varphi = 0$, see Section 2.

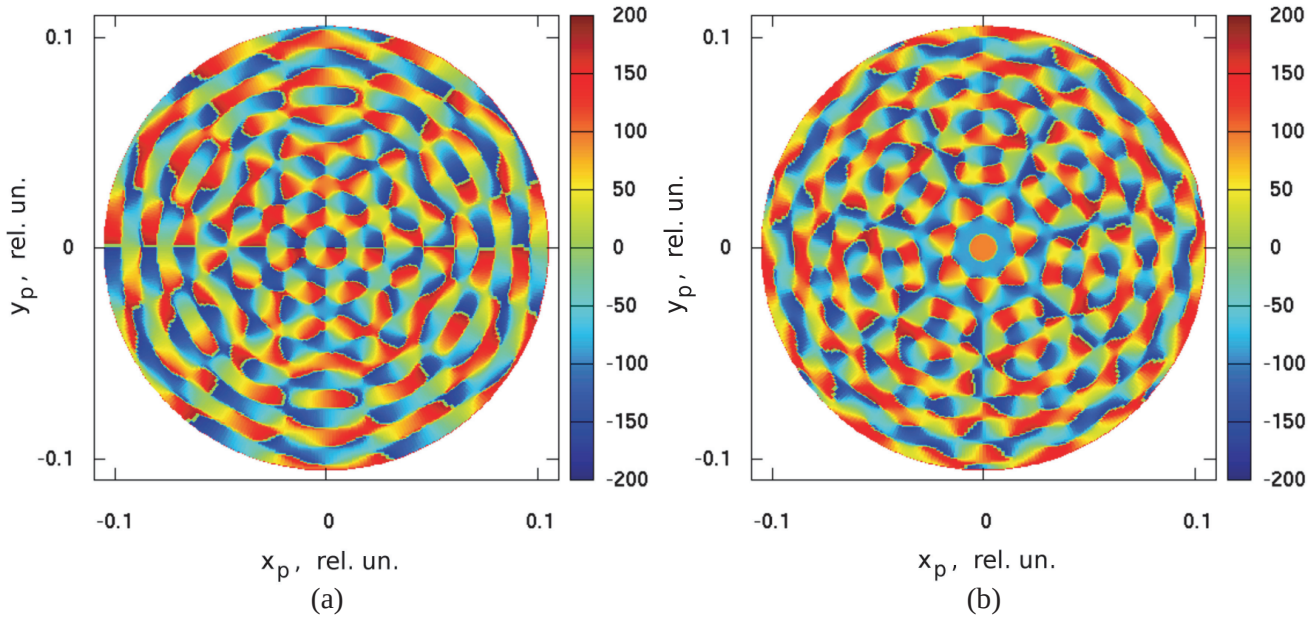


Figure 11. Phase pattern of the E_{x_p} far-field component of the beam of (a) Fig. 8(a) and (b) Fig. 8(b).

The effect of a limited number of antenna patches in a ring array is shown in Figs. 12 and 13. Fig. 12 shows the far-field power pattern of a tilted beam from a source of the same kind as in Fig. 6(b) where, instead of a continuous ring, an array of (a) $N = 72$ and (b) $N = 36$ point-like antenna elements is used. The source creates the beam of azimuthal polarization ($g_{0rn} = 0$, $a = 0.6\,\mathrm{m}$, $\lambda = 1\,\mathrm{cm}$) with the phase factor of Eq. (24) at $n = 8$, $m = 1$, $s = 2.8$, $\tau = 0$. In this case, the spacing between the antenna elements is (a) $L_a = 5.2\,\mathrm{cm}$ and (b) $L_a = 10.4\,\mathrm{cm}$, respectively.

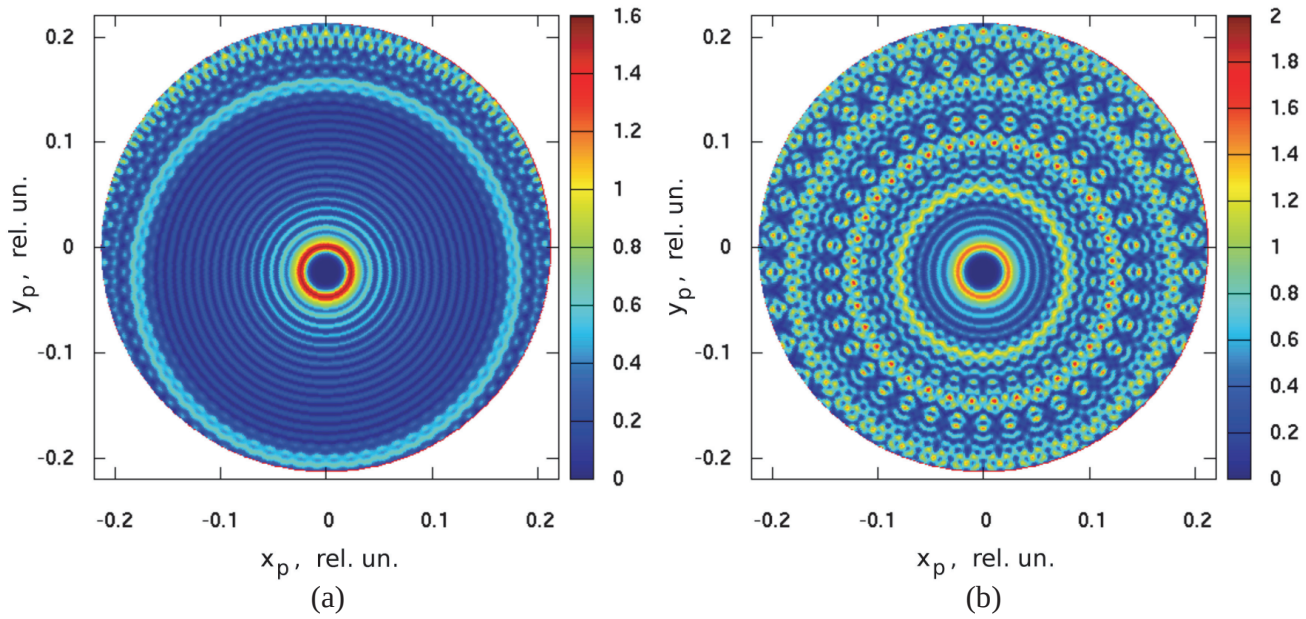


Figure 12. Far-field power pattern of the beam from a ring source of the kind as in Fig. 6(b) when the source is an array of (a) $N = 72$ and (b) $N = 36$ point-like antenna elements rather than a continuous ring ($a = 0.6\,\mathrm{m}$).

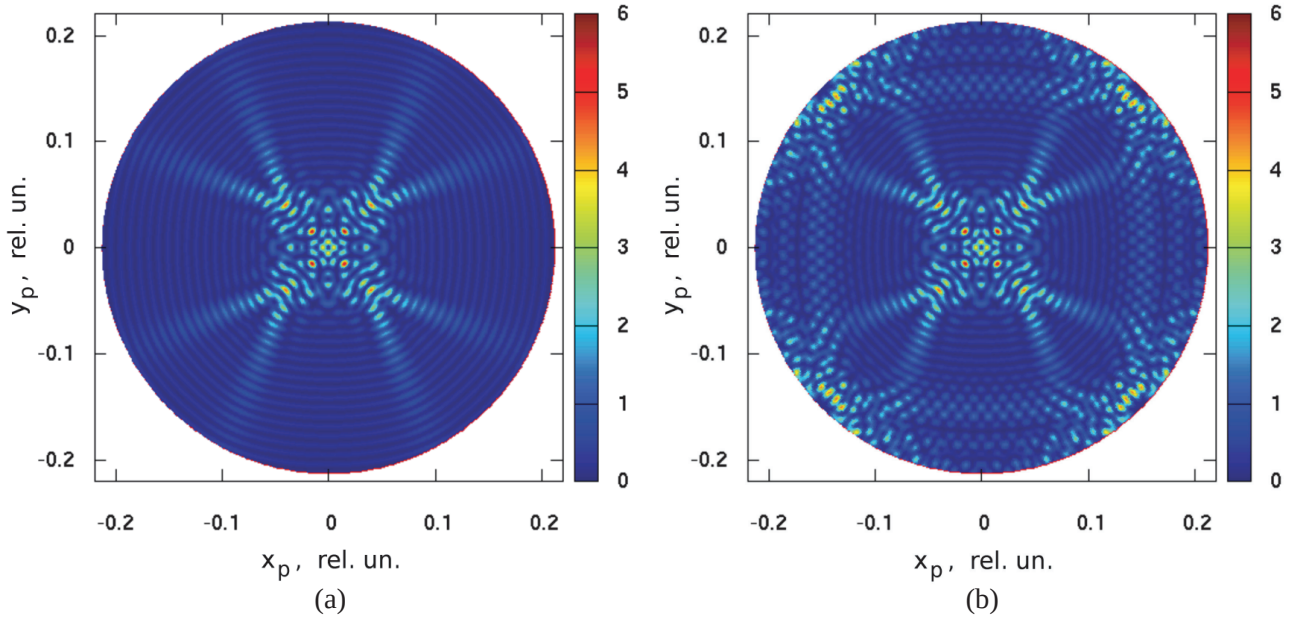


Figure 13. Fractured far-field power pattern of the beam from a ring array of (a) $N = 720$ and (b) $N = 72$ point-like antenna elements rather than a continuous ring of the kind defined by Eq. (12) (circular polarization of $(-)$ sign) with the phase factor of Eq. (24) at $a = 0.6\,\mathrm{m}$, $\lambda = 1\,\mathrm{cm}$, $n = 8$, $m = 4$, $s = 1$, $\tau = 0$).

For the comparison, Fig. 13 shows the far-field pattern of a fractured beam of circular polarization of $(-)$ sign emitted by the array of (a) $N = 720$ and (b) $N = 72$ antenna elements ($a = 0.6\,\mathrm{m}$, $\lambda = 1\,\mathrm{cm}$, $n = 8$, $m = 4$, $s = 1$, $\tau = 0$). In this case, the spacing is (a) $L_a = 0.52\,\mathrm{cm}$ and (b) $L_a = 5.2\,\mathrm{cm}$.

The analysis shows that, even at a small number of patches in the array when the spacing between patches may exceed the wavelength, the central part of the beam is nearly the same as in the case of a continuous ring. The size of the preserved central part is, though, getting smaller with reducing the number of patches (increasing the spacing L_a).

Figure 14 shows the effect of the power drop along the array in the source considered in Fig. 12(a) at $m = 0$ (no beam tilt). Any patch (a point-like antenna element) is assumed to radiate a fraction δP of the feed power supplied by the microstrip line. When the number of patches is large, e.g., $N = 72$ as in Fig. 14, the value of δP has to be small for the patches to radiate in a reasonably uniform manner.

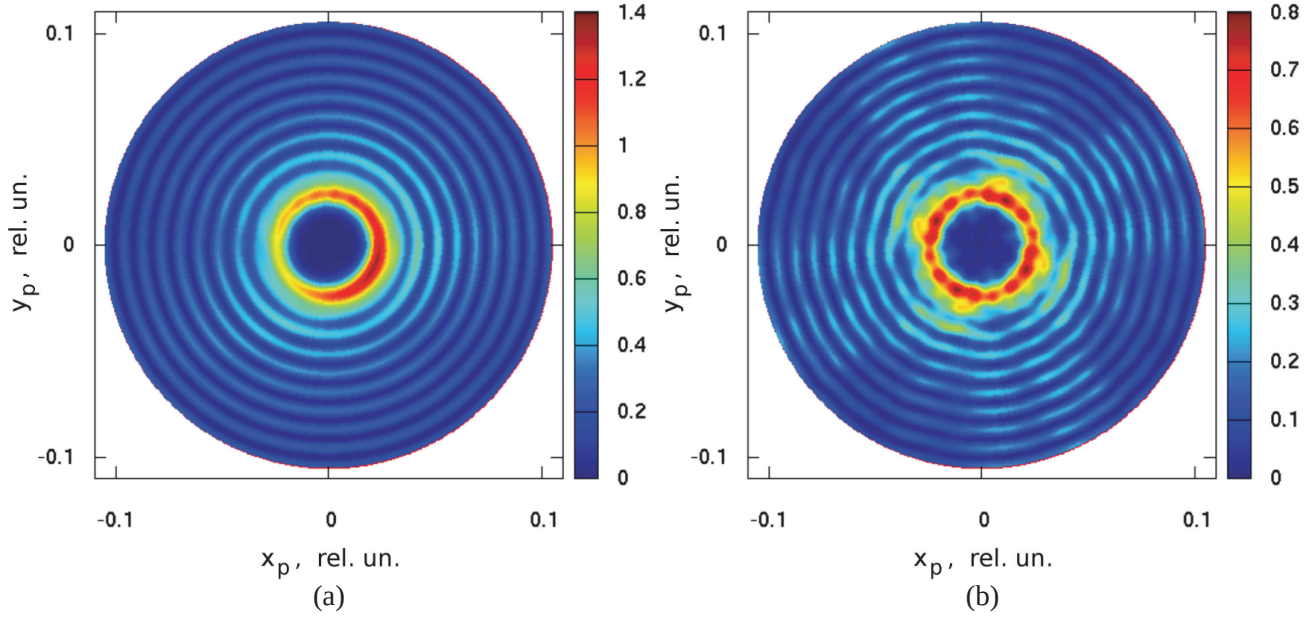


Figure 14. Far-field power pattern of the beam from a ring source of Fig. 12 having $N = 72$ patches (azimuthal polarization, $a = 0.6\,\mathrm{m}$, $\lambda = 1\,\mathrm{cm}$, $n = 8$, $m = 0$) with radiation efficiency per patch (a) $\delta P = -20\,\mathrm{dB}$ and (b) $\delta P = -10\,\mathrm{dB}$ when using one and four feed points, respectively.

Figure 14(a) shows that, with a single feed point, for the beam to nearly preserve the axial symmetry, the radiation efficiency of each patch should be as low as $\delta P = -20\,\mathrm{dB}$ ($a = 0.6\,\mathrm{m}$, $n = 8$, $m = 0$). In this case, the radiation power of the last patch drops to 0.49 of the power of the first one. If the radiation efficiency δP is relatively high, a few feed points could improve the situation. Fig. 14(b) shows the beam from the array with four feed points exciting four sections of 18 patches each, respectively, at the patch radiation efficiency $\delta P = -10\,\mathrm{dB}$. In this case, the radiation power of the last patch of each section drops to 0.17 of the radiation power of the first patch (the one at the feed point).

Implementation of the phase function $f_n(\varphi'; m, s, \tau)$ could be either (a) dynamic, via the phase control of each antenna patch, or (b) static, via the pre-defined φ'-dependence of the length of microstrip lines between patches j and $j+1$ located at the angular positions φ'_j and φ'_{j+1}, respectively,

$$L_r(\varphi'_j) = L_\varphi(\varphi'_j) = L_{0n} + \delta L \sin\left(m(\varphi'_j - \tau)\right) \tag{25}$$

where L_{0n} is the mean length providing the phase delay $\Delta\Phi_n = 2\pi(1 + n/N)$ between the adjacent patches for the n-th order beam, and δL is the amplitude of the length variation proportional to s.

Fractured beams could provide potential benefits for radar applications when tracing a target with a central beam and scanning the neighborhood with a set of m rotating sub-beams. In this case, focusing the power of sub-beams into m spots rather than smearing it over ring sidelobes allows one to increase and better localize the radar response from any sub-target close to the main target being observed.

5. CONCLUSIONS

We simulated near and far fields of microwave vortex beams emitted by the Bessel-kind finite-aperture and ring sources of radial, azimuthal, and circular polarizations.

A patch antenna array of circular shape and special feed has been proposed for exciting the beams with phase-shift and frequency-sweep control of angular modes and polarization patterns. The effects of limited number of patches and gradual drop of power along the array have been considered.

A periodic azimuthal undulation of helical wavefront of the OAM beams has been proposed as a new form of the phase-modified vortex beams. This allows one to significantly diversify and dynamically control the structure of the OAM beams and their quantitative parameters. The latter can provide a range of potential benefits such as the following:

1. Introduction of additional degrees of freedom for the dynamic control of the vortex beams that increases the diversity of spatial configurations of beams.

2. A possibility of spatial encoding of information via the dynamic variation of the OAM beam structure.

3. Extension of radar capabilities through the use of fractured vortex-tilted rotating sub-beams, which help to better localize sub-targets in the vicinity of the main target being observed.

Other benefits may be found in further research.

ACKNOWLEDGMENT

The work was partially supported by The Scientific and Technological Research Council of Turkey (TUBITAK) through the 2221 Fellowship Program for Visiting Scientists and Scientists on Sabbatical Leave (2019/6).

REFERENCES

1. Shen, Y., X. Wang, Z. Xie, C. Min, X. Fu, Q. Liu, M. Gong, and X. Yuan, "Optical vortices 30 years on: OAM manipulation from topological charge to multiple singularities," *Light: Science & Applications*, Vol. 8, No. 90, 2019.
2. Lee, D., H. Sasaki, H. Fukumoto, K. Hiraga, and T. Nakagawa, "Orbital Angular Momentum (OAM) multiplexing: An enabler of a new era of wireless communications," *IEICE Trans. Commun.*, Vol. E100-B, 1044–1063, 2017.
3. Mao, F., M, Huang, J. Yang, C. Yang, T. Li, and J. Zhang, "Capacity performance of wireless OAM-based massive MIMO system," *Progress In Electromagnetics Research M*, Vol. 82, 149–156, 2019.
4. Chen, R., H. Zhou, M. Moretti, X. Wang, and J. Li, "Orbital angular momentum waves: Generation, detection, and emerging applications," *IEEE Commun. Surveys Tuts.*, Vol. 22, 840–868, 2020.
5. Zheng, F., Y. Chen, S, Ji, and G. Duan, "Research status and prospects of orbital angular momentum technology in wireless communication," *Progress In Electromagnetics Research*, Vol. 168, 113–132, 2020.
6. Yagi, Y., H. Sasaki, T. Yamada, and D. Lee, "200 Gb/s wireless transmission using dual-polarized OAM-MIMO multiplexing with uniform circular array on 28 GHz band," *IEEE Antennas Wireless Propag. Lett.*, Vol. 20, 833–837, 2021.
7. Varzakas, P., "Average channel capacity for Rayleigh fading spread spectrum MIMO systems," *International Journal of Communication Systems*, Vol. 19, 1081–1087, 2006.
8. Liu, K., Y. Cheng, X. Li, H. Wang, Y. Qin, and Y. Jiang, "Study on the theory and method of vortex-electromagnetic-wave-based radar imaging," *IET Microwaves Antennas and Propagation*, Vol. 10, 961–968, 2016.
9. Tang, B., J. Bai, and K.-Y. Guo, "Bi-target tracking based on vortex wave with orbital angular momentum," *Progress In Electromagnetics Research C*, Vol. 74, 123–129, 2017.

10. Fang, Y., J. Chen, P. Wang, C. Li, and W. Liu, "A novel image formation method for electromagnetic vortex SAR with orbital-angular-momentum," *Progress In Electromagnetics Research M*, Vol. 82, 129–137, 2019.
11. Zhang, K., Y. Wang, Y. Yuan, and S. N. Burokur, "A review of orbital angular momentum vortex beams generation: from traditional methods to metasurfaces," *Appl. Sci.*, Vol. 10, 1015, 2020.
12. Byun, W.-J., B. S. Kim, Y.-S. Lee, M. S. Kang, K. S. Kim, and Y. H. Cho, "Simple generation of orbital angular momentum modes with azimuthally deformed Cassegrain subreflector," *Electron. Lett.*, Vol. 51, No. 19, 1480–1482, 2015.
13. Zheng, S., X. Hui, X. Jin, H. Chi, and X. Zhang, "Transmission characteristics of a twisted radio wave based on circular traveling-wave antenna," *IEEE Trans. Antennas Propag.*, Vol. 63, No. 4, 1530–1536, 2015.
14. Liu, W., H. Cheng, J. Tian, and S. Chen, "Diffractive metalens: From fundamentals, practical applications to current trends," *Advances in Physics: X*, Vol. 5, No. 1, 1742584, 2020.
15. Zhang, K., Y. Yuan, D. Zhang, X. Ding, B. Ratni, S. N. Burokur, M. Lu, K. Tang, and Q. Wu, "Phase-engineered metalenses to generate converging and non-diffractive vortex beam carrying orbital angular momentum in microwave region," *Opt. Express*, Vol. 26, No. 2, 1351–1360, 2018.
16. Li, J.-S. and J.-Z. Chen, "Multi-beam and multi-mode orbital angular momentum by utilizing a single metasurface," *Opt. Express*, Vol. 29, No. 17, 27332–27339, 2021.
17. Huang, H.-F. and H.-M. Huang, "Millimeter-wave wideband high efficiency circular Airy OAM multibeams with multiplexing OAM modes based on transmission metasurfaces," *Progress In Electromagnetics Research*, Vol. 173, 151–159, 2022.
18. Mohammadi, S. M., L. K. S. Daldorff, J. E. S. Bergman, R. L. Karlsson, B. Thide, K. Forozesh, T. D. Carozzi, and B. Isham, "Orbital angular momentum in radio - a system study," *IEEE Trans. Antennas Propag.*, Vol. 58, No. 2, 565–572, 2010.
19. Mazzinghi, A., M. Balma, D. Devona, G. Guarnieri, G. Mauriello, M. Albani, and A. Freni, "Large depth of field pseudo-Bessel beam generation with a RLSA antenna," *IEEE Trans. Antennas Propag.*, Vol. 62, 3911–3919, 2014.
20. Wei, W., K. Mahdjoubi, C. Brousseau, and O. Emile, "Generation of OAM waves with circular phase shifter and array of patch antennas," *Electron. Lett.*, Vol. 51, No. 6, 441–443, 2015.
21. Liu, K., H. Liu, Y. Qin, Y. Cheng, S. Wang, X. Li, and H. Wang, "Generation of OAM beams using phased array in the microwave band," *IEEE Trans. Antennas Propag.*, Vol. 64, 3850–3857, 2016.
22. Lin, M., Y. Gao, P. Liu, and J. Liu, "Theoretical analyses and design of circular array to generate orbital angular momentum," *IEEE Trans. Antennas Propag.*, Vol. 65, No. 7, 3510–3519, 2017.
23. Liu, D., L. Gui, Z. Zhang, H. Chen, G. Song, and T. Jiang, "Multiplexed OAM wave communication with two-OAM-mode antenna systems," *IEEE Access*, Vol. 7, 4160–4166, 2019.
24. Padgett, M. J., F. M. Miatto, M. P. J. Lavery, A. Zeilinger, and R. W. Boyd, "Divergence of an orbital-angular-momentum-carrying beam upon propagation," *New J. Phys.*, Vol. 17, 023011, 2015.
25. Xu, J., K. Bi, R. Zhang, Y. Hao, C. Lan, K. D. McDonald-Maier, X. Zhai, Z. Zhang, and S. Huang, "A small-divergence-angle orbital angular momentum metasurface antenna," *AAAS Research*, Vol. 2019, 9686213, 2019.
26. Fuscaldo, W., A. Benedetti, D. Comite, P. Burghignoli, P. Baccarelli, and A. Galli, "Microwave synthesis of Bessel, Bessel-Gauss, and Gaussian beams: A fully vectorial electromagnetic approach," *Int. J. Microwave Wireless Technol.*, Vol. 13, 509–516, 2021.
27. Balanis, C. A., *Advanced Engineering Electromagnetics*, Wiley, New York, 1989.
28. Maffei, B., F. Noviello, J. A. Murphy, P. A. R. Ade, J.-M. Lamarre, F. R. Bouchet, J. Brossard, A. Catalano, R. Colgan, R. Gispert, E. Gleeson, C. V. Haynes, W. C. Jones, A. E. Lange, Y. Longval, I. McAuley, F. Pajot, T. Peacocke, G. Pisano, J.-L. Puget, I. Ristorcelli, G. Savini, R. Sudiwala, R. J. Wylde, and V. Yurchenko, "Planck pre-launch status: HFI beam expectations from the optical optimisation of the focal plane," *Astron. Astrophys.*, Vol. 520, A12, 2010.

29. Rosset, C., V. B. Yurchenko, J. Delabrouille, J. Kaplan, Y. Giraud-Heraud, J.-M. Lamarre, and J. A. Murphy, "Beam mismatch effects in cosmic microwave background polarization measurements," *Astronomy and Astrophysics*, Vol. 464, No. 1, 405–415, 2007.
30. Yurchenko, V. B. and J.-M. Lamarre, "Efficient computation of the broadband beam sidelobes exemplified by the Planck high-frequency instrument," *J. Opt. Soc. Am. A*, Vol. 22, No. 12, 2838–2846, 2005.
31. Yurchenko, V. B., J. A. Murphy, and J.-M. Lamarre, "Fast physical optics simulations of the multi-beam dual-reflector submillimeter-wave telescope on the ESA Planck Surveyor," *International Journal of Infrared and Millimeter Waves*, Vol. 22, No. 1, 173–184, 2001.
32. Hernandez-Figueroa, H. E., M. Zamboni-Rached, and E. Recami, Eds., *Localized Waves*, Wiley-Interscience, IEEE Press, Hoboken, N.J., 2008.
33. Albani, M., S. C. Pavone, M. Casaletti, and M. Ettorre, "Generation of non-diffractive Bessel beams by inward cylindrical traveling wave aperture distributions," *Opt. Express*, Vol. 22, No. 15, 18354–18364, 2014.
34. Ciydem, M. and E. A. Miran, "Dual polarization wideband sub-6 GHz suspended patch antenna for 5G base station," *IEEE Antennas Wireless Propag. Lett.*, Vol. 19, 1142–1146, 2020.